SOFT MATERIALS FOR UNCONVENTIONAL ADHESIVES AND ELECTRONICS

Michael D. Bartlett
Assistant Professor of Materials Science and Engineering
Iowa State University
Ames, IA

Abstract
Multifunctional soft materials create intriguing new opportunities to enhance performance and enable innovative designs. I will present two examples of this approach, one that utilizes material composition through liquid-solid hybrid composites for soft machines and deformable electronics and another inspired by kirigami, the art of paper cutting, where material structures are manipulated to create materials with tunable functionality. For hybrid composites, I will present an all-soft matter approach that combines soft elastomers with dispersions of liquid-phase eutectic Ga-In (EGaIn) metal alloy microdroplets. Experimental and theoretical investigations show that liquid metal droplets incorporated into elastomers enables exceptional combinations of soft elasticity and electrical and thermal properties with extreme toughness, autonomously self-healing circuits, and mechanically triggered stiffness tuning.[1,2] For kirigami, I will present a framework for designing materials with highly tunable mechanical and adhesive properties.[3,4] This is demonstrated with hybrid cut architectures to create highly tunable mechanical properties, stretchable conductors, and rapid magnetoactive soft actuators which elongate to 330 % strain in $\sim$0.1 s. Furthermore, by incorporating kirigami-inspired structures at interfaces, we can enhance adhesive force by a factor of 100 across a spatially patterned sheet while tuning adhesion in different directions for high capacity yet easy release interfaces. These approaches provide model systems to study fundamental material properties while enabling electronic skins, soft robots, and 'smart' adhesives for a variety of soft matter systems.

1 Liquid metal composites

Soft materials that sense, actuate, self-heal, and actively tune properties provide opportunities to create highly multifunctional materials.[5–7] This allows for material systems that are highly deformable and mechanically tunable and robust across diverse length scales. The ability for functional materials to bend, stretch, and twist is typically accomplished by utilizing elastomeric substrates as a carrier for active materials. This approach is highly versatile and amendable to diverse materials including deterministically patterned metal wires or 'wavy' circuitry,[8,9] networks of conductive nanomaterials such as carbon nanotubes and graphene,[10,11] and conductive and semi-conducting polymers.[12,13] Another method is to use non-toxic liquid metal (LM) alloys such as Galinstan or eutectic gallium indium (EGaIn). This approach has led to highly elastic circuitry,[14] tunable antennas,[15,16] and deformation sensors.[17,18] The use of a conductive liquid combines the desirable electrical and thermal properties of metal with the deformability and softness of fluids, providing an intriguing option for multifunctional soft materials. Such materials can be useful for a variety of applications, including soft robotics[19–21] and "artificial skin" electronics for bio-monitoring and human-machine interaction.[11,22,23]

Previously, the author and other researchers have shown that LM-embedded elastomer (LMEE) composites can be engineered to exhibit a wide range of material properties – from

dielectric insulators[24] with high thermal conductivity[25–27] and toughness[28] to electric conductors[29–32] that autonomously form new conductive pathways when the material is torn, punctured, or removed.[33] Here we present the thermal and mechanical properties of liquid, solid, and liquid-solid multiphase soft elastomer composites. We incorporate a series of spherical, solid microparticles including iron (Fe), copper (Cu), silver (Ag), and nickel (Ni) into LM(EGaIn) and then disperse this suspension in a soft, highly extensible silicone elastomer. We find modest increases in thermal conductivity for multiphase systems with significant stiffening and reductions in stretchability. Contrary to solid particles, LM inclusions can be incorporated into composites with much greater volume which enables significantly enhanced thermal conductivities while displaying greater extensibility and lower stiffness. Composites consisting only of liquid filler can be loaded up to $\phi = 80\%$ ($\phi = \frac{vol(total filler)}{vol(composite)}$) with thermal conductivities up to $k = 6.7 \pm 0.1\ W \cdot m^{-1} \cdot K^{-1}$ while still being electrically insulating. Taking advantage of the extensibility of the LM elastomer systems, we stretch an electrically insulating LM composite with $\phi = 60\%$ (sample with appreciable thermal conductivity and relatively high stretchability) and develop thermal conductivity values as high as $11.0 \pm 0.5\ W \cdot m^{-1} \cdot K^{-1}$ in the stretching direction at strains of 400%.

1.1 Results and Discussion

Three primary composite compositions are investigated, i) LM inclusions, ii) solid particles, and iii) multiphase composites consisting of LM inclusions and solid particles **(Figure 1** a-c). In all cases, the matrix phase is a highly extensible silicone elastomer (Gelest Ex-Sil 100) and the LM is eutectic gallium indium (EGaIn), where $\phi = 0\%$ represents the unmodified elastomer (no additional filler). The solid particles in the multiphase composites are Fe, Ag, Cu, or Ni, all of which have a diameter of 1 μm and the LM inclusions generally have an average major radii of 10 - 15 μm. The composites are fabricated by shear mixing uncured elastomer with the different fillers. For multiphase composites, the solid particles are mixed into the LM, and then this suspension is mixed into the uncured elastomer phase. The composites are then cast, cured, and prepared for mechanical and thermal testing. Mechanical properties are evaluated under tension on composite films in a dogbone geometry. The thermal conductivity is measured using a transient hot wire (THW) technique in which a 25 μm diameter platinum wire is placed between two slabs of the material to be measured.

Mechanical and thermal characterization of the three types of composites is presented in Figure 1d-f. Here, the multiphase composites are comprised of solid filler:LM in a 1:1 ratio by volume. It is found that solid particles and multiphase systems where the solid particles alloy (Cu) with the LM result in the stiffest materials with the lowest strain at break, the LM+Fe 1:1 composite which does not alloy displays moderate stiffness and strain at break, while the LM composite is significantly softer and more extensible than both systems for any given volume loading. We also found that higher volume loadings of solid particles and multiphase composites cause incomplete wetting of the particles in our system, which results in granular and paste-like materials which are too brittle for mechanical testing. This was observed in the ϕ = 40% Fe, ϕ = 50% LM+Fe, and ϕ = 40% LM+Cu samples, accounting for the absence of mechanical test data for these materials in Figure 1. Thermal conductivity is measured and is found to be similar for all the three types of composites up to $\phi = 40\%$, with the multiphase LM + Cu displaying a slightly increased thermal conductivity ($k = 1.9 \pm 0.1\ W \cdot m^{-1} \cdot K^{-1}$) compared to the other materials ($k \approx 1.5\ W \cdot m^{-1} \cdot K^{-1}$). However, it is found that the liquid inclusions can be loaded to

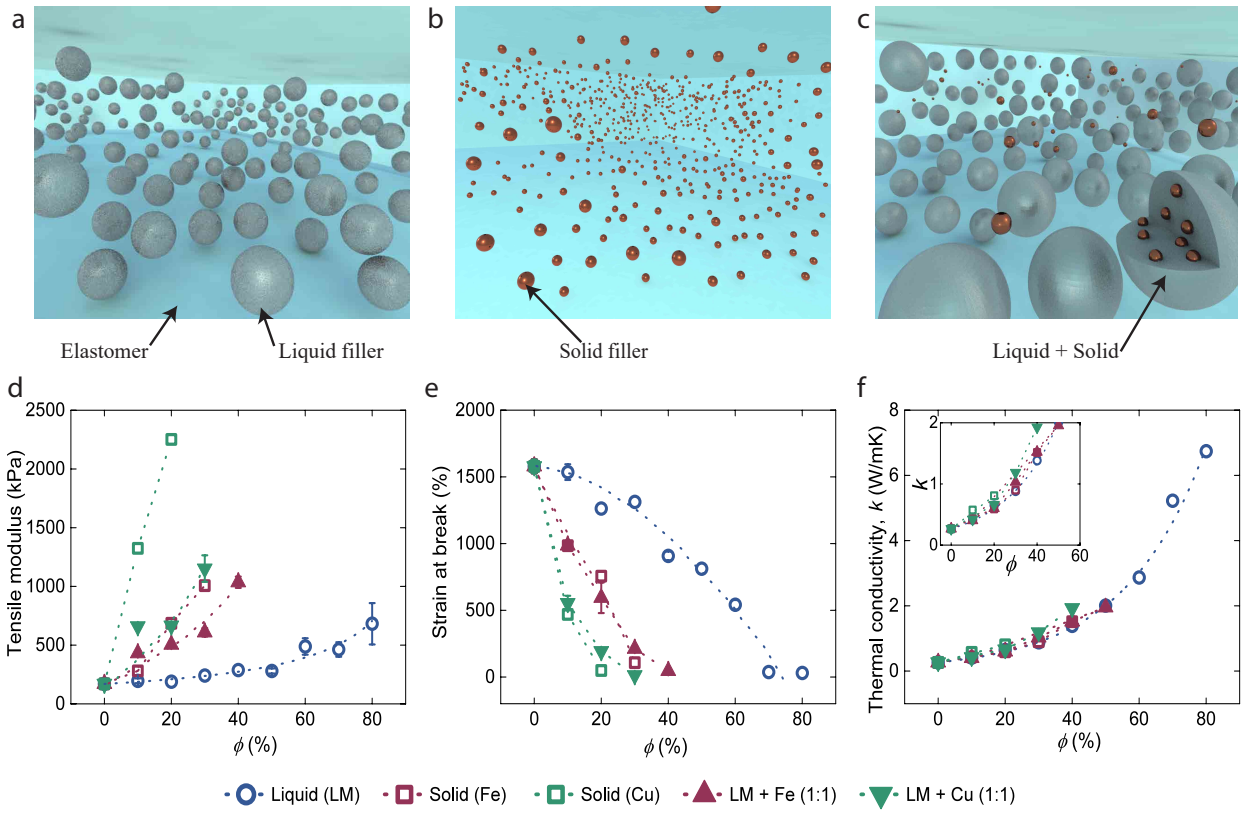

Figure 1: Mechanical and thermal properties for soft composites. Schematics of a) liquid, b) solid, and c) liquid-solid multiphase composite, where relative particle size is based on the average particle radius found through particle analysis, with LM droplets and solid particles on the order of 10 - 15 μm and 1 μm respectively. d-f) Tensile modulus, Strain at break and Thermal conductivity, all with respect to total volume percent filler (ϕ). Inset in (f) shows the region where $k \leq 2\ W \cdot m^{-1} \cdot K^{-1}$. Dashed lines are guides to the eye. All error bars represent ± 1 SD and are not displayed if smaller than the data point size. Tensile modulus and strain at break of ϕ = 40% Fe, ϕ = 50% LM+Fe, and ϕ = 40% LM+Cu samples are not plotted due to the brittleness of the samples leading to testing inability.

significantly higher loadings ($\phi = 80\%$) compared to the solid phase alone ($\phi = 30\%$) while still being an elastic solid. The higher LM loading ($\phi = 80\%$) allows the thermal conductivity to be increased to $k = 6.7 \pm 0.1\ W \cdot m^{-1} \cdot K^{-1}$, well beyond the solid or multiphase composite while still being relatively soft (tensile modulus $\approx$ 680 kPa) and deformable (strain at break $\approx$ 30%). These results demonstrate that when the multiphase composites are mixed with equal volume of solid and liquid fillers, the soft mechanical response degrades faster than the thermal conductivity increases.

To evaluate the thermal conductivity under strain, we modify the THW setup to stretch the elastomer while thermal conductivity is measured both transverse and along the direction of stretch. These measurements can then be decomposed into the orthotropic thermal conductivity values of the bulk material (k_x, k_y, k_z), where k_y is defined as the stretching direction (**Figure 2**a). Here we find that the unfilled elastomer ($\phi = 0\%$) displays a constant thermal conductivity in the

direction of stretch of $k_y \approx 0.3\ W \cdot m^{-1} \cdot K^{-1}$. When a LM composite ($\phi = 60\%$) is stretched, k_y increases as strain is increased up to 400% strain where $k_y = 11.0 \pm 0.5\ W \cdot m^{-1} \cdot K^{-1}$ (Figure 2b). This value is one of the highest reported for an electrically insulating, soft composite material. To model this behavior we utilize a modified Bruggeman formulation that allows for predictions of thermal conductivity as a function of strain by considering the change in aspect ratio of the LM droplets during stretching.[34] In Figure 2c, we plot k/k_0 as a function of strain for the $\phi = 60\%$ LM composite in the k_y and k_x directions. The model well predicts the behavior where k_y increases and k_x shows a slight decrease upon stretching. This prediction is achieved without any fitting parameters and captures the strain dependent thermal conductivity of the elastomer-LM composite.

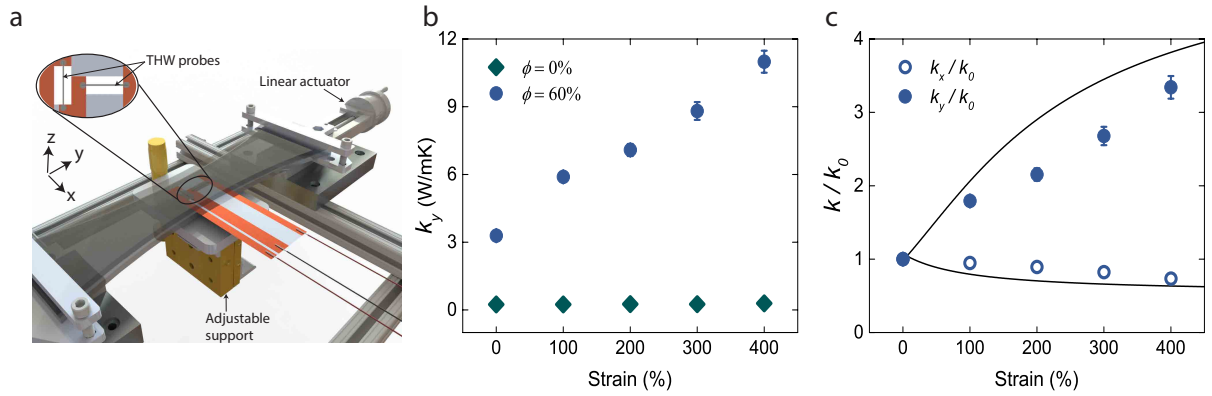

Figure 2: Thermal-mechanical coupling. a) Schematic of the stretching experiment setup with THW probe in the inset b) Absolute values of thermal conductivity in the direction of stretch for an unfilled elastomer ($\phi = 0\%$) and a LM composite ($\phi = 60\%$). c) Strain vs normalized thermal conductivity along the direction and transverse direction of stretch where the solid lines represent theoretical predictions. All error bars represent ± 1 SD and are not displayed if smaller than the data point size.

To demonstrate the thermal-mechanical coupling behavior we embed resistive heaters in the elastomers and use an infrared camera to monitor the change in temperature upon turning the heating element on and off. Two volume fractions ($\phi = 0\%, 60\%$) and two strains ($50\%, 275\%$) are chosen to illustrate the effect of filler and strain (See **Figure 3**a). Each sample consists of two halves activated using oxygen plasma, stretched to the predetermined strain and bonded to the resistive heating wire (Nichrome wire) on either side (Figure 3b). The samples are connected in series to a power supply to maintain a constant current. The average temperature of regions at the center of each sample (square regions in first IR image in Figure 3a) are monitored over time and plotted in Figure 3c. When a constant current (600 mA) is supplied to this system at t = 0 s, the unfilled elastomer ($\phi = 0\%$) reaches a higher temperature and at a faster rate compared to the LM composites. Furthermore, when the power supply is turned off, the LM composite at 275% strain shows a more rapid decrease in temperature relative to both the LM composite at lower strain (50%) and the unfilled elastomer. This demonstration shows how both the composition and applied strain influence heat conduction and the potential for these soft-composites for use in stretchable electronics, soft robotics, and programmable matter where combinations of thermal conductivity and mechanical compliance are required.

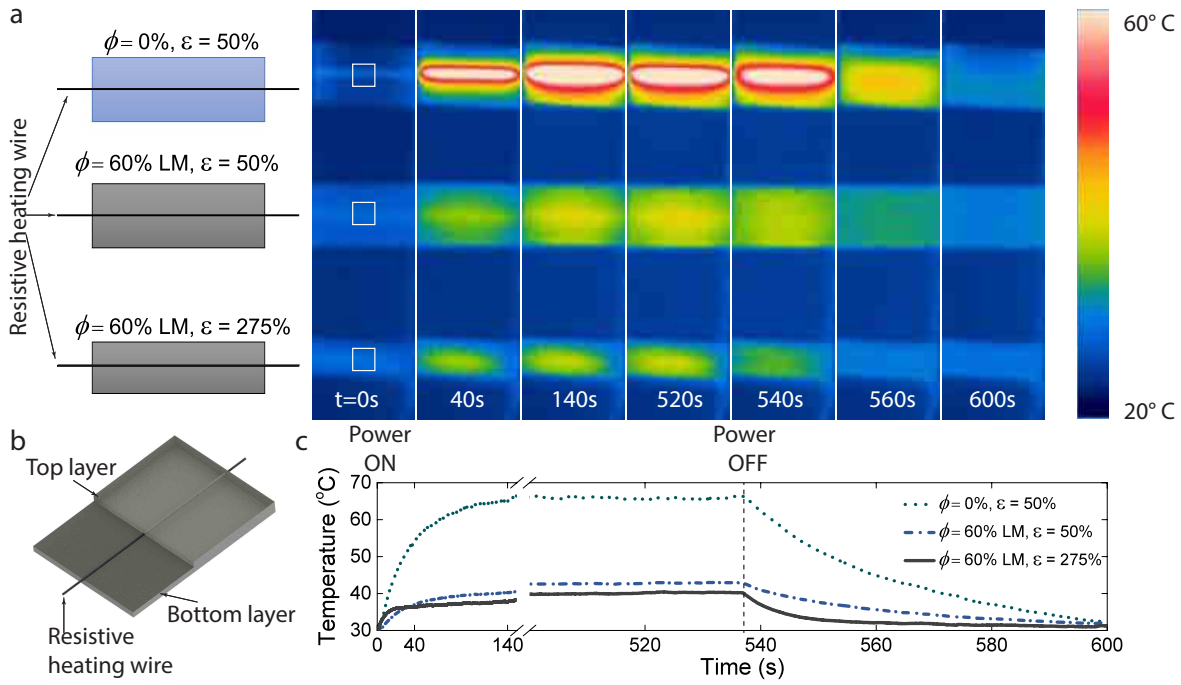

Figure 3: Resistive heating demonstration with infrared imaging. a) Schematic of the samples used for demonstration with LM filler volume fractions ($\phi = 0\%, 60\%$ and 60%) and strains ($50\%, 50\%$ and 275%) respectively. Squares in the first IR image show the region in each sample where the temperature was monitored. b) Schematic showing the sectional view of a sample bonded on either side of a resistive heating wire (both halves are similar in dimensions, a section of the top half is cut out to show the details). c) Plot showing the average temperature in the monitored regions as a function of time as the resistive heaters are powered on and off.

2 Kirigami-inspired Structures for Smart Adhesion

The art of paper cutting, often known as kirigami and jiǎnzhǐ, can be applied to engineer materials with unique functional properties such as elastic softening, high extensibility and the creation of complex 3D morphologies, through designed cuts.[35–39] This approach has been implemented to enhance functionality of diverse material sets, leading to a spectrum of smart electronics and sensors.[40–46] Although there have been many reports on the mechanical behavior of kirigami structures and their potential functional applications, the influence of incisions or the complete removal of film materials at interfaces has not been well explored. With the ability to tune mechanics and structure through cuts, kirigami-inspired designs offer great potential to control adhesion and wetting through the precise control of interfacial properties.

Here we show that kirigami-inspired structures at interfaces provide a mechanism to spatially control and enhance adhesion strength while providing directional characteristics for high capacity, easy release interfaces. Kirigami-inspired adhesives are created by introducing cuts through rapid laser machining into continuous adhesive films consisting of elastomeric interfaces supported by inextensible films. Although cutting films has been utilized in various art forms, we choose to describe the presented patterns as kirigami-inspired as we utilize repeating cut patterns

in continuous films with interconnected structures, which are characteristics of kirigami design. We study the peel adhesion response of these systems by varying interconnect structure and interfacial geometry. This approach introduces spatially varying regions of stiff and compliant regions which allows for the systematic tuning of bending rigidity and actual contact width. As cracks propagate through these regions a material defined characteristic length scale is found to dictate force enhancement, where above a critical length bending rigidity and actual contact width can be tuned in stiff and compliant regions to enhance adhesive force capacity by a factor of $\sim$100 across a sheet. The influence of interconnects on adhesion is further investigated and as the number on interconnects increases, the adhesive force decreases and approaches that of a homogeneous strip as the bending rigidity contrast between stiff and compliant regions decreases. Furthermore, we demonstrate the anisotropic properties of kirigami-inspired adhesives, where peeling along orthogonal directions results in anisotropic adhesive ratios of $\sim$10. These experimental results are supported by theoretical predictions in which the bending rigidity and actual contact width of kirigami-inspired interconnects and structures are found to drive adhesive capacity. This model well describes the experimental data and provides general design criteria for diverse kirigami-inspired adhesive structures. These structures and design criteria open new possibilities for advanced adhesive functionality, including spatially controlled systems, wearable electronics, and anisotropic bandages that enable strong adhesive capacity and easy release, which we demonstrate with a skin mounted kirigami-inspired adhesive strip.

2.1 Results and Discussion

Three different adhesive designs are created to investigate the effect of kirigami-inspired structures on peel adhesion (Figure 4a-c). Each design consists of alternating stiff and compliant regions of equal thickness, which are made of an adhesive layer and encapsulation layer of polydimethylsiloxane (PDMS) (E = 880 $\pm$ 40 kPa) separated by a inextensible polyethylene terephthalate (PET) strip (E = 2.6 $\pm$ 0.1 GPa). In both regions, the PDMS serves as the adhesive layer. Model A consists of alternating sections of discrete stiff and compliant regions, where the PET sheet is absent in the compliant region. Model B introduces stiff interconnects, which bridge across the compliant regions to connect the stiff regions. Model C is designed by eliminating the PDMS regions between interconnects in the compliant regions, creating an open structure. Initially, there are three interconnects, one at each edge and another in the center of the strip. The adhesive strips are examined with 90° peel adhesion measurements, where the interfacial crack propagates through the alternating compliant/stiff regions.

To optimally design kirigami-inspired adhesives the relative size and geometry of the stiff and compliant regions needs to be controlled. We consider the heterogeneous kirigami-inspired adhesive as a repeating array of unit cells with a compliant and a stiff region. The stiff region is characterized by width w_s, length l_s, and thickness t_s, which consists of a PET sheet t_{PET} and two encapsulating PDMS layers t_{PDMS}. The width and thickness of the stiff region are constant throughout the experiment (w_s = 46 mm, t_s = 0.75 $\pm$ 0.1 mm). The length l_s = 2, 4, 8, 12, 20 mm is selected based on the characteristic length of the stiff region ($l_{ch,s} = \sqrt{\frac{2E_cI_c}{wG_c}} \approx 6.4$ mm), where the characteristic length l_{ch} is a length scale comparable to the dimension of the stress field at the peel front.[47] If l_s is smaller than $l_{ch,s}$ the peel front propagates from a compliant region to a stiff region without fully undergoing the crack arresting effect, which reduces adhesion enhancement. The compliant region is characterized by width w_c, length l_c, and thickness t_c in the same manner.

To quantitatively explain the adhesion enhancement of kirigami-inspired adhesives we

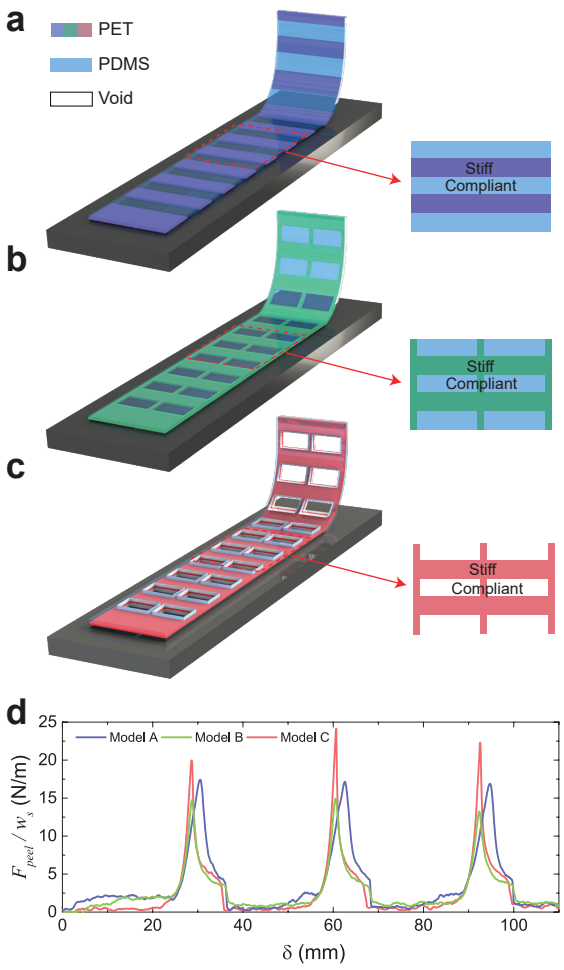

Figure 4: a-c) Schematics of kirigami-inspired adhesives, which consist of alternating stiff and compliant regions, under 90° peel loading. (a) The compliant region of Model A is continuous, whereas (b) Model B incorporates rigid interconnects on the continuous layer and (c) Model C consists of interconnects supported by an adhesive with voids between interconnects. d) A representative normalized peel force versus displacement plot for each model.

follow a fracture mechanics energy balance approach. For a homogeneous adhesive strip under a 90° peel loading the crack propagates with a steady state peel force with $F_{peel} = wG_c$, where w is the strip width and G_c is the critical strain energy release rate for interfacial fracture.[48] However, for a heterogeneous strip, the peel force in the compliant region (F_c) and stiff region (F_s) vary as the crack propagates into the interface between these regions. This interface modifies the shape of the bent adhesive strip, which changes the mechanical energy in the system.[47,49] The change in shape depends on the bending rigidity (EI) of the two regions, where E is the elastic modulus and I is the second moment of area. Additionally, for the case of kirigami-inspired adhesives, the actual contact width changes as the crack travels across the interface from w_c to w_s. In this framework, the effective adhesion enhancement ratio of peel force is calculated by considering

the variation of total energy such that:

$$\frac{F_s}{F_c} = \frac{E_s I_s w_s}{E_c I_c w_c} \tag{2.1}$$

where the subscripts s and c denote the stiff and compliant terms respectively. Equation 2.1 shows that the enhancement ratio of kirigami-inspired adhesives is controlled by the difference in bending stiffness *EI* and actual contact width *w* in both regions.

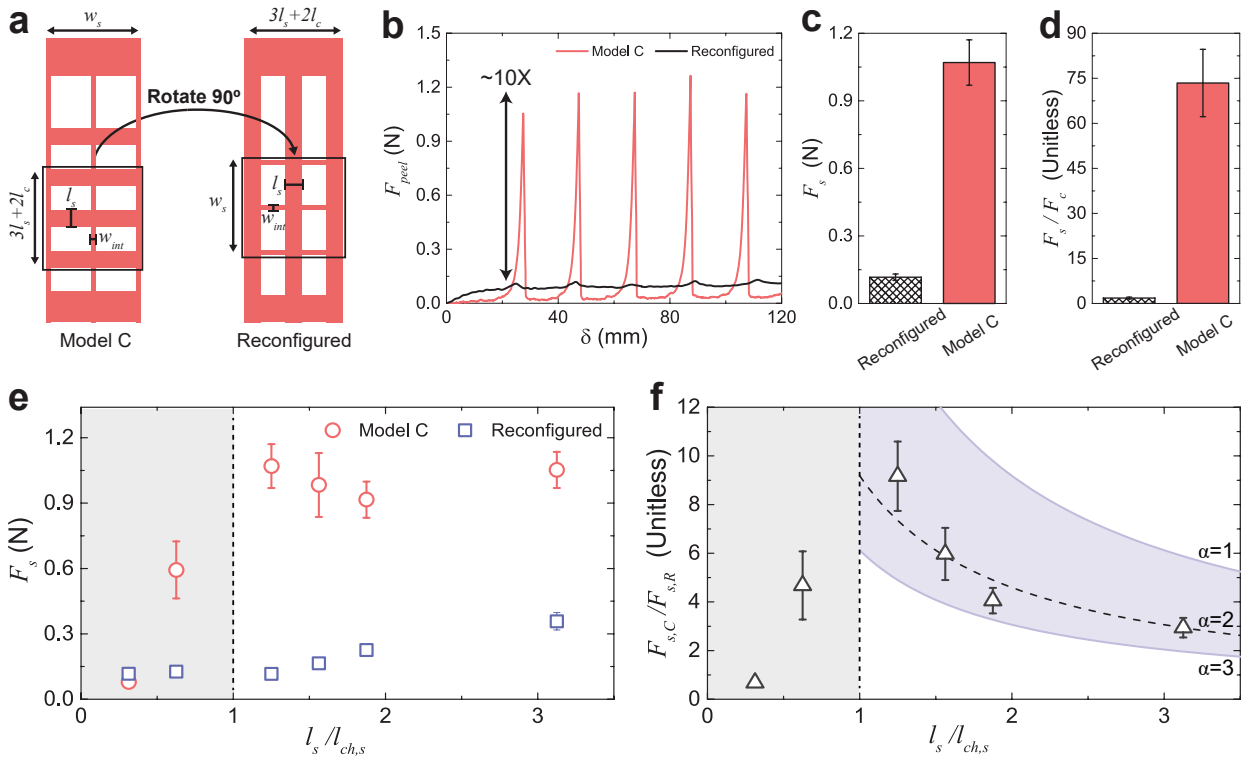

Figure 5: a) Schematic diagram of a Model C adhesive and a directionally reconfigured adhesive. b) F_{peel} versus displacement plot for a Model C and reconfigured adhesive. c) F_s and d) adhesion enhancement ratio (F_s/F_c) for Model C and the reconfigured model. l_s = 8 mm for components *a-d*. e) F_s versus $l_s/l_{ch,s}$ where l_s is varied from 2 to 20 mm. f) Adhesion anisotropy ratio ($F_{s,C}/F_{s,R}$) versus $l_s/l_{ch,s}$ where the lines are the predictions from Equation 2 with the specified α values and the blue shading represents the region within these limits. Grey regions in *e* and *f* represent regions where $l_s/l_{ch,s} < 1$. All adhesives within the figure have three interconnects (N=3).

Due to the directional nature of the kirigami structures, kirigami-inspired adhesives are expected to display anisotropic adhesive characteristics. This is investigated by selecting a unit cell in the Model C design and rotating 90 degrees with constant dimensions to create a reconfigured model (Figure 5a). Figure 5b shows a plot of normalized peel force as a function of displacement for a Model C adhesive and a directionally reconfigured adhesive (l_s = 8 mm and w_{int} = 2 mm). The average peak force of the Model C design is ∼10x higher than those of the reconfigured model. Figure 5c and d summarize these results by plotting the peak force F_s and the adhesion enhancement ratio F_s/F_c of the two directionally contrasting designs. It is shown that when cuts are perpendicular to the crack propagation direction, the peak force and

enhancement ratio are high. Alternatively, the reconfigured model has cuts parallel to the crack propagation direction, resulting in a low peak force and enhancement ratio. This is due to two primary factors. First, Model C meets the criterion $l_s > l_{ch,s}$, while the reconfigured design does not, resulting in enhanced crack trapping and adhesion enhancement for Model C. Second, the actual contact width in the compliant region for Model C is reduced, where $w_c = 0.13w_s$ while the reconfigured structure has $w_c = 0.50w_s$.

To design cut patterns for anisotropic adhesion we consider the following criteria. For Model C, $l_s \geq l_{ch,s}$ and $w_{int} << l_{ch,s}$, this will result in an increased $F_{s,C}$ and a decreased $F_{c,C}$, where we introduce the second subscript to denote the design. Upon reconfiguring Model C (90 degree rotation), the slender interconnects from Model C become the stiff regions in the reconfigured model, where due to the condition that $w_{int} < l_{ch,s}$, the crack will not fully arrest and $F_{s,R}$ will be reduced. Further, the contact width at the stiff interface in the reconfigured model should be minimized while still allowing for crack arrest in Model C, here we find that $l_{s,C} \simeq l_{ch,s}$. To quantify this effect, first we define the adhesion anisotropy ratio as $F_{s,C}/F_{s,R}$ where $F_{s,C}$ is the peak force in Model C and $F_{s,R}$ is the peak force in the reconfigured model. Given the conditions above, the stiffness variation in the reconfigured model is reduced and approximations are made such that $w_{s,R} = w_{c,R}$ and $F_{s,R} = \alpha F_{c,R}$, where α describes the magnitude of crack arrest in the reconfigured model with $\alpha = 1$ representing a minimized crack arresting response. Upon rearranging Equation 2.1 to $F_{s,C} = (E_s I_s w_s / E_c I_c w_c) F_{c,C}$ and substituting the respective F_s terms into the adhesion anisotropy ratio, we find that for $l_s \geq l_{ch,s}$:

$$\frac{F_{s,C}}{F_{s,R}} = \frac{E_s I_s w_s}{E_c I_c L_s \alpha} \tag{2.2}$$

where $L_s = \sum_{i=1}^{N_R} l_{s,i}$ and N_R is the number of rotated stiff segments in the reconfigured model. This shows that the adhesion anisotropy ratio is inversely proportional to l_s when $l_s \geq l_{ch,s}$, demonstrating that for maximum anisotropy ratios, l_s should be approximately equal to $l_{ch,s}$ to provide enhancement in Model C while minimizing peel width during removal of the reconfigured Model. This is experimentally examined by varying l_s across the range $0.31 l_{ch,s} \leq l_s \leq 3.1 l_{ch,s}$ for Model C and the reconfigured model and measuring $F_{s,C}$ and $F_{s,R}$. As seen in Figure 5e, $F_{s,C}$ increases until $l_s/l_{ch,s} \simeq 1$ at which point $F_{s,C}$ reaches a plateau value, while $F_{s,R}$ increases throughout the $l_s/l_{ch,s}$ range as the peel width increases. Therefore, when looking at the adhesion anisotropy ratio ($F_{s,C}/F_{s,R}$) in Figure 5f, a maximum value is obtained when $l_s/l_{ch,s} \simeq 1$ and then decreases as l_s increases. When Equation 2.2 is plotted with three different α values, the data is best described by $\alpha = 2$, demonstrating that modest crack arrest occurs at the stiff regions in the reconfigured model. By further minimizing crack arrest by decreasing w_{int} the adhesion anisotropy ratio could be further enhanced. These experiments and analysis demonstrate that through designed layouts of elasticity and interconnects, kirigami-inspired adhesives with desired anisotropic properties can be created.

To examine the general behavior of kirigami-inspired adhesives relative to the theoretical predictions from Equation 2.1, we plot the adhesion enhancement ratio (F_s/F_c) as a function of the bending stiffness and the width ratio ($E_s I_s w_s/E_c I_c w_c$) in Figure 6a. The plot shows excellent agreement between the experimental data and Equation 2.1 without any data fitting parameters. When an adhesive is homogeneous, there is no enhancement in peak force (F_s = F_c). In contrast, when a periodic layout of kirigami-inspired patterns is introduced onto the adhesive, periodic

undulations of peel force are observed ($F_s > F_c$). The adhesion enhancement ratio F_s/F_c of the kirigami-inspired adhesives varies by a factor of $\sim$100 relative to a homogeneous adhesive. For the case of Model B and C, experimental data points are distributed along the prediction line, which depends on the number of interconnects in the compliant regions. The peak force F_s and the adhesion enhancement ratio F_s/F_c decrease with an increasing number of interconnects as the heterogeneous system becomes more similar to a homogeneous strip. A deviation from this prediction is observed for Model C with a single interconnect (N = 1), where the theory over predicts the experimental value. We attribute this deviation to the poor load sharing across the single interconnect. These results provide a general design criteria for kirigami-inspired adhesives under peel loading, where further tuning of interfacial structure such as changing thickness, interconnect geometry, or materials could lead to greater enhancements and control of adhesion force.

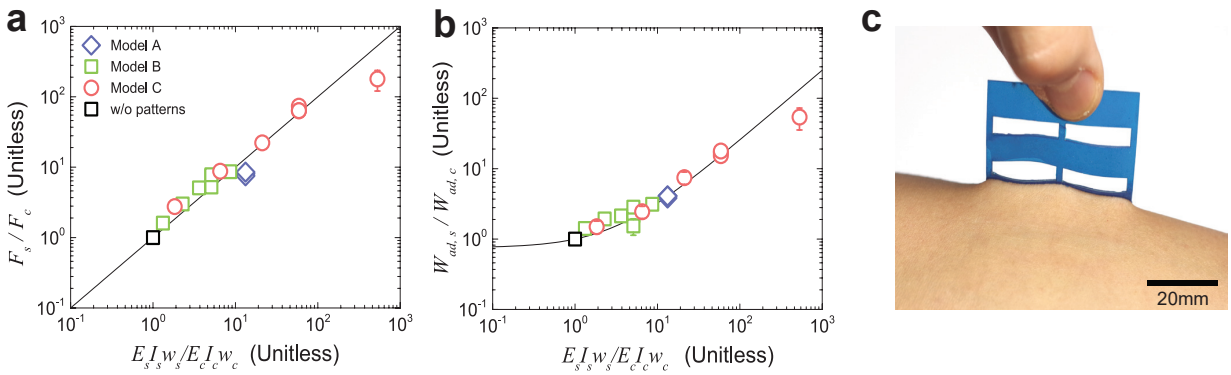

Figure 6: a) Log-log plot of the adhesion enhancement ratio (F_s/F_c) versus the contrast in bending stiffness and width ($E_sI_sw_s/E_cI_cw_c$), where the solid line is the prediction from Equation 2.1. b) Log-log plot of the enhancement ratio in work of adhesion versus $E_sI_sw_s/E_cI_cw_c$, the solid line is an empirical fit with y=1/4x + 3/4. In both figures, data points that do not meet the length criterion $l_s > l_{ch,s}$ are excluded. c) Photograph of a kirigami-inspired adhesive peeling off of an arm.

We also compute the work of adhesion W_{ad} of kirigami-inspired adhesives, which represents the work done by an external loading system during the creation of new surfaces between the adhesive and substrate.[50] The work of adhesion when a peel front crosses a stiff interface is given by calculating the area under the curve of a peel force-displacement plot such that $\frac{1}{w_s(\delta_p-\delta_0)}\int_{\delta_0}^{\delta_p} F(\delta)d\delta$, where δ_0 is the displacement at which the crack begins transversing a stiff interface and δ_p is displacement at the peak force. The enhancement ratio in work of adhesion $W_{ad,s}/W_{ad,c}$ as a function of $E_sI_sw_s/E_cI_cw_c$ is presented in Figure 6b, where $W_{ad,s}/W_{ad,c}$ increases as $E_sI_sw_s/E_cI_cw_c$ increases. Here we find $\frac{W_{ad,s}}{W_{ad,c}} \approx \frac{1}{4}\frac{E_sI_sw_s}{E_cI_cw_c}$, which shows that the enhancement in work of adhesion increases at a slower rate that than the enhancement in force with respect to $E_sI_sw_s/E_cI_cw_c$. This difference in the scaling for force and work of adhesion provides a mechanism to increase force capacity without expending excess energy during separation. This could be useful for applications such as climbing robots where adhesive capacity is desirable for supporting loads without large amounts of energy consumption during locomotion.

These results provide guidance for the design and implementation for new classes of adhesive materials. We believe this work will be useful for bandages and wearable electronics, where adhesion to skin can be controlled spatially and directionally. Additionally, as functional

kirigami devices find uses in skin mounted applications, the principals developed here can provide insight into component placement and interfacial structure for controlled and strong adhesion. To highlight this potential, a kirigami-inspired adhesive is mounted on the arm in Figure 6c. When peeled perpendicular to the cuts, a high resistance to peeling is observed at every compliant-to-stiff interface, however, it is easily peeled off when the cuts are parallel to the peeling direction, as the peel front propagates without meeting a stiff interface, as demonstrated in the anisotropic results in Figure 5. This proof-of-concept for spatially controlled and anisotropic adhesives demonstrates a path for high capacity, easy-release dry bandages and wearable devices.

References

[1] Boyce S. Chang, Ravi Tutika, Joel Cutinho, Stephanie Oyola-Reynoso, Jiahao Chen, Michael D. Bartlett, and Martin M. Thuo. Mechanically triggered composite stiffness tuning through thermodynamic relaxation (ST3R). *Materials Horizons*, 5(3):416–422, 2018.

[2] Ravi Tutika, Shihuai H. Zhou, Ralph E. Napolitano, and Michael D. Bartlett. Mechanical and Functional Tradeoffs in Multiphase Liquid Metal, Solid Particle Soft Composites. *Advanced Functional Materials*, page 201804336, 2018.

[3] Doh-Gyu Hwang and Michael D. Bartlett. Tunable Mechanical Metamaterials through Hybrid Kirigami Structures. *Scientific Reports*, 8(1):3378, 2018.

[4] Doh-Gyu Hwang, Katie Trent, and Michael D. Bartlett. Kirigami-inspired Structures for Smart Adhesion. *ACS Applied Materials & Interfaces*, 10(7):6747–6754, 2018.

[5] Michael Andrew McEvoy and Nikolaus Correll. Materials that couple sensing, actuation, computation, and communication. *Science*, 347(6228):1261689, 2015.

[6] Michael Wehner, Ryan L Truby, Daniel J Fitzgerald, Bobak Mosadegh, George M Whitesides, Jennifer A Lewis, and Robert J Wood. An integrated design and fabrication strategy for entirely soft, autonomous robots. *Nature*, 536(7617):451–455, 2016.

[7] Pedro M Reis, Heinrich M Jaeger, and Martin van Hecke. Designer matter: A perspective. *Extreme Mechanics Letters*, 5:25–29, 2015.

[8] Yugang Sun, Won Mook Choi, Hanqing Jiang, Yonggang Y Huang, and John A Rogers. Controlled buckling of semiconductor nanoribbons for stretchable electronics. *Nature nanotechnology*, 1(3):201, 2006.

[9] Sheng Xu, Yihui Zhang, Lin Jia, Kyle E Mathewson, Kyung-In Jang, Jeonghyun Kim, Haoran Fu, Xian Huang, Pranav Chava, Renhan Wang, et al. Soft microfluidic assemblies of sensors, circuits, and radios for the skin. *Science*, 344(6179):70–74, 2014.

[10] Liliane Bokobza and Colette Belin. Effect of strain on the properties of a styrene–butadiene rubber filled with multiwall carbon nanotubes. *Journal of applied polymer science*, 105(4):2054–2061, 2007.

[11] Mallory L Hammock, Alex Chortos, Benjamin C-K Tee, Jeffrey B-H Tok, and Zhenan Bao. 25th anniversary article: the evolution of electronic skin (e-skin): a brief history, design considerations, and recent progress. *Advanced materials*, 25(42):5997–6038, 2013.

[12] Jie Xu, Sihong Wang, Ging-Ji Nathan Wang, Chenxin Zhu, Shaochuan Luo, Lihua Jin, Xiaodan Gu, Shucheng Chen, Vivian R Feig, John WF To, et al. Highly stretchable polymer semiconductor films through the nanoconfinement effect. *Science*, 355(6320):59–64, 2017.

[13] Jin Young Oh, Simon Rondeau-Gagné, Yu-Cheng Chiu, Alex Chortos, Franziska Lissel, Ging-Ji Nathan Wang, Bob C Schroeder, Tadanori Kurosawa, Jeffrey Lopez, Toru Katsumata, et al. Intrinsically stretchable and healable semiconducting polymer for organic transistors. *Nature*, 539(7629):411, 2016.

[14] Mohammed G Mohammed and Rebecca Kramer. All-printed flexible and stretchable electronics. *Adv. Mater.*, 29(19), 2017.

[15] Shi Cheng, Zhigang Wu, Paul Hallbjorner, Klas Hjort, and Anders Rydberg. Foldable and stretchable liquid metal planar inverted cone antenna. *IEEE Transactions on antennas and propagation*, 57(12):3765–3771, 2009.

[16] Ju-Hee So, Jacob Thelen, Amit Qusba, Gerard J Hayes, Gianluca Lazzi, and Michael D Dickey. Reversibly deformable and mechanically tunable fluidic antennas. *Advanced Functional Materials*, 19(22):3632–3637, 2009.

[17] Hyun-Joong Kim, Chulwoo Son, and Babak Ziaie. A multiaxial stretchable interconnect using liquid-alloy-filled elastomeric microchannels. *Applied Physics Letters*, 92(1):011904, 2008.

[18] Yong-Lae Park, Carmel Majidi, Rebecca Kramer, Phillipe Bérard, and Robert J Wood. Hyperelastic pressure sensing with a liquid-embedded elastomer. *Journal of Micromechanics and Microengineering*, 20(12):125029, 2010.

[19] Cecilia Laschi, Barbara Mazzolai, and Matteo Cianchetti. Soft robotics: Technologies and systems pushing the boundaries of robot abilities. *Sci. Robot.*, 1(1):eaah3690, 2016.

[20] Steven I Rich, Robert J Wood, and Carmel Majidi. Untethered soft robotics. *Nature Electronics*, 1(2):102, 2018.

[21] Jian Wu, Shi-Yang Tang, Tao Fang, Weihua Li, Xiangpeng Li, and Shiwu Zhang. A wheeled robot driven by a liquid-metal droplet. *Advanced Materials*, page 1805039, 2018.

[22] Tran Quang Trung and Nae-Eung Lee. Flexible and stretchable physical sensor integrated platforms for wearable human-activity monitoringand personal healthcare. *Advanced materials*, 28(22):4338–4372, 2016.

[23] Michael D Bartlett, Eric J Markvicka, and Carmel Majidi. Rapid fabrication of soft, multilayered electronics for wearable biomonitoring. *Advanced Functional Materials*, 26(46):8496–8504, 2016.

[24] Michael D Bartlett, Andrew Fassler, Navid Kazem, Eric J Markvicka, Pratiti Mandal, and Carmel Majidi. Stretchable, high-k dielectric elastomers through liquid-metal inclusions. *Advanced Materials*, 28(19):3726–3731, 2016.

[25] Seung Hee Jeong, Si Chen, Jinxing Huo, Erik Kristofer Gamstedt, Johan Liu, Shi-Li Zhang, Zhi-Bin Zhang, Klas Hjort, and Zhigang Wu. Mechanically stretchable and electrically insulating thermal elastomer composite by liquid alloy droplet embedment. *Scientific reports*, 5:18257, 2015.

[26] Michael D Bartlett, Navid Kazem, Matthew J Powell-Palm, Xiaonan Huang, Wenhuan Sun, Jonathan A Malen, and Carmel Majidi. High thermal conductivity in soft elastomers with elongated liquid metal inclusions. *Proc. Natl Acad Sci. USA*, page 201616377, 2017.

[27] Ravi Tutika, Shihuai H Zhou, Ralph E Napolitano, and Michael D Bartlett. Mechanical and functional tradeoffs in multiphase liquid metal, solid particle soft composites. *Advanced Functional Materials*, page 1804336, 2018.

[28] Navid Kazem, Michael D Bartlett, and Carmel Majidi. Extreme toughening of soft materials with liquid metal. *Advanced Materials*, page 1706594, 2018.

[29] Andrew Fassler and Carmel Majidi. Liquid-phase metal inclusions for a conductive polymer composite. *Advanced Materials*, 27(11):1928–1932, 2015.

[30] Jiangxin Wang, Guofa Cai, Shaohui Li, Dace Gao, Jiaqing Xiong, and Pooi See Lee. Printable superelastic conductors with extreme stretchability and robust cycling endurance enabled by liquid-metal particles. *Advanced Materials*, 30(16):1706157, 2018.

[31] Zhe Yu, Jie Shang, Xuhong Niu, Yiwei Liu, Gang Liu, Pravarthana Dhanapal, Yanan Zheng, Huali Yang, Yuanzhao Wu, Youlin Zhou, et al. A composite elastic conductor with high dynamic stability based on 3d-calabash bunch conductive network structure for wearable devices. *Advanced Electronic Materials*, page 1800137, 2018.

[32] Suqing Liang, Yaoyao Li, Yuzhen Chen, Jinbin Yang, Taipeng Zhu, Deyong Zhu, Chuanxin He, Yizhen Liu, Stephan Handschuh-Wang, and Xuechang Zhou. Liquid metal sponges for mechanically durable, all-soft, electrical conductors. *J. Mater. Chem. C*, 5(7):1586–1590, 2017.

[33] Eric J Markvicka, Michael D Bartlett, Xiaonan Huang, and Carmel Majidi. An autonomously electrically self-healing liquid metal–elastomer composite for robust soft-matter robotics and electronics. *Nature materials*, 17(7):618–624, 2018.

[34] Michael D. Bartlett, Navid Kazem, Matthew J Powell-palm, Xiaonan Huang, and Wenhuan Sun. High thermal conductivity in soft elastomers with elongated liquid metal inclusions. *Proceedings of the National Academy of Sciences*, 114(9):2143–2148, 2017.

[35] Paul Z. Hanakata, Zenan Qi, David K. Campbell, and Harold S. Park. Highly stretchable MoS2 kirigami. *Nanoscale*, 8(1):458–463, 2016.

[36] Daniel M. Sussman, Yigil Cho, Toen Castle, Xingting Gong, Euiyeon Jung, Shu Yang, and Randall D. Kamien. Algorithmic lattice kirigami: A route to pluripotent materials. *Proceedings of the National Academy of Sciences*, 112(24):7449–7453, 2015.

[37] T. Castle, D. M. Sussman, M. Tanis, and R. D. Kamien. Additive lattice kirigami. *Science Advances*, 2(9):e1601258–e1601258, 2016.

[38] Toen Castle, Yigil Cho, Xingting Gong, Euiyeon Jung, Daniel M. Sussman, Shu Yang, and Randall D. Kamien. Making the cut: Lattice kirigami rules. *Physical Review Letters*, 113(24):245502, 2014.

[39] Terry C. Shyu, Pablo F. Damasceno, Paul M. Dodd, Aaron Lamoureux, Lizhi Xu, Matthew Shlian, Max Shtein, Sharon C. Glotzer, and Nicholas A. Kotov. A kirigami approach to engineering elasticity in nanocomposites through patterned defects. *Nature Materials*, 14(8):785–789, 2015.

[40] Y Iwata and E Iwase. Stress-Free Stretchable Electronic Device. *Micro Electro Mechanical Systems (MEMS)*, 2017 IEEE:231–234, 2017.

[41] Zeming Song, Xu Wang, Cheng Lv, Yonghao An, Mengbing Liang, Teng Ma, David He, Ying-Jie Zheng, Shi-Qing Huang, Hongyu Yu, and Hanqing Jiang. Kirigami-based stretchable lithium-ion batteries. *Scientific Reports*, 5:10988, 2015.

[42] Takao Someya, Yusaku Kato, Tsuyoshi Sekitani, Shingo Iba, Yoshiaki Noguchi, Yousuke Murase, Hiroshi Kawaguchi, and Takayasu Sakurai. Conformable, flexible, large-area networks of pressure and thermal sensors with organic transistor active matrixes. *Proceedings of the National Academy of Sciences of the United States of America*, 102(35):12321–12325, 2005.

[43] Aaron Lamoureux, Kyusang Lee, Matthew Shlian, Stephen R Forrest, and Max Shtein. Dynamic kirigami structures for integrated solar tracking. *Nature Communications*, 6:8092, 2015.

[44] Hengyu Guo, Min Hsin Yeh, Ying Chih Lai, Yunlong Zi, Changsheng Wu, Zhen Wen, Chenguo Hu, and Zhong Lin Wang. All-in-One Shape-Adaptive Self-Charging Power Package for Wearable Electronics. *ACS Nano*, 10(11):10580–10588, 2016.

[45] Y. Yamamoto, Shingo Harada, Daisuke Yamamoto, Wataru Honda, Takayuki Arie, S. Akita, and K. Takei. Printed multifunctional flexible device with an integrated motion sensor for health care monitoring. *Science Advances*, 2(11):e1601473–e1601473, 2016.

[46] Biswajit Saha, Sangwoong Baek, and Junghoon Lee. Highly Sensitive Bendable and Foldable Paper Sensors Based on Reduced Graphene Oxide. *ACS Applied Materials & Interfaces*, 9(5):4658–4666, 2017.

[47] K. Kendall. Control of cracks by interfaces in composites. 246(1247):539–555, 1975.

[48] K. Kendall. Thin-film peeling-the elastic term. *Journal of Physics D: Applied Physics*, 8:1449–1452, 1975.

[49] S. Xia, L. Ponson, G. Ravichandran, and K. Bhattacharya. Toughening and Asymmetry in Peeling of Heterogeneous Adhesives. *Physical Review Letters*, 108(19):196101, 5 2012.

[50] A. V. Pocius D. A. Dillard. *Adhesion science and engineering: surfaces, chemistry and applications.* Elsevier, 2002.